

Decomposition of Fe-Ni Martensite: Implications for the Low-Temperature (≤ 500 °C) Fe-Ni Phase Diagram

J. ZHANG, D.B. WILLIAMS, and J.I. GOLDSTEIN

The low-temperature (< 500 °C) decomposition of Fe-Ni martensite was studied by aging martensitic Fe-Ni alloys at temperatures between 300 °C and 450 °C and by measuring the composition of the matrix and precipitate phases using the analytical electron microscope (AEM). For aging treatments between 300 °C and 450 °C, lath martensite in 15 and 25 wt pct Ni alloys decomposed with γ [face-centered cubic (fcc)] precipitates forming intergranularly, and plate martensite in 30 wt pct Ni alloys decomposed with γ (fcc) precipitates forming intragranularly. The habit plane for the intragranular precipitates is $\{111\}_{fcc}$ parallel to one of the $\{110\}_{bcc}$ planes in the martensite. The compositions of the γ intergranular and intragranular precipitates lie between 48 and 58 wt pct Ni and generally increase in Ni content with decreasing aging temperature. Diffusion gradients are observed in the matrix α [body-centered cubic (bcc)] with decreasing Ni contents close to the martensite grain boundaries and matrix/precipitate boundaries. The Ni composition of the matrix α phase in decomposed martensite is significantly higher than the equilibrium value of 4 to 5 wt pct Ni, suggesting that precipitate growth in Fe-Ni martensite is partially interface reaction controlled at low temperatures (< 500 °C). The results of the experimental studies modify the $\gamma/\alpha + \gamma$ phase boundary in the present low-temperature Fe-Ni phase diagram and establish the eutectoid reaction in the temperature range between 400 °C and 450 °C.

I. INTRODUCTION

MARTENSITE [body-centered cubic (bcc)] forms upon cooling in the Fe-rich region of the Fe-Ni phase diagram.^[1] Figure 1 shows the Fe-Ni phase diagram^[2] and the variation of the martensite start temperature (M_s) with Ni content. When martensite is aged in the two-phase $\alpha + \gamma$ field, the equilibrium γ [face-centered cubic (fcc)] phase precipitates from the martensite matrix and the martensite matrix transforms into the α (bcc) phase.^[2,3] The composition of the γ and α phases formed above ~ 500 °C has been measured using the electron probe microanalyzer (EPMA) and the analytical electron microscope (AEM).^[2,3] It has been argued that the α and γ phases formed by martensite decomposition are in equilibrium, since the phase compositions are the same at specific aging temperatures and no concentration gradients are observed in either α or γ . Using these data, the $\gamma/\alpha + \gamma$ and $\alpha/\alpha + \gamma$ phase boundaries in the Fe-rich portion of the Fe-Ni phase diagram above ~ 450 °C to 500 °C were determined.^[2,3]

At low temperatures (< 500 °C), the decomposition of martensite, α_2 , becomes more complicated, in part because the diffusivity of Fe and Ni in α and γ is very low. As a result of the low diffusion coefficients, the precipitates which are formed are very small, typically ~ 50 -nm wide at 400 °C and ~ 10 -nm wide at 300 °C for a 1-year heat treatment.^[2] The accurate measurement of

the γ precipitate composition requires analytical instruments that provide a very high spatial resolution. In addition to the small precipitate size, the alloys are usually not fully equilibrated within a practical time period at the low temperatures. As a result, composition gradients are also present in the matrix.

Based on the measurement of phase boundary compositions in iron meteorites,^[4] electron irradiation experiments of Fe-Ni alloys,^[5] and thermodynamic calculations,^[6] a low-temperature Fe-Ni phase diagram has been proposed,^[7] as shown in Figure 2. This phase diagram adopts the high-temperature $\alpha + \gamma$ two-phase boundaries^[2] from Figure 1 and incorporates the calculated eutectoid and the tricritical point.^[6] The ordering temperatures and the low Ni spinodal boundary were determined from the *in situ* electron irradiation experiments.^[5] Below about 450 °C, the high-temperature γ phase splits into the low Ni paramagnetic γ_1 and high Ni ferromagnetic γ_2 phases. The eutectoid composition, the α and γ'' (FeNi) phase boundaries below 400 °C, the miscibility gap boundaries, and the spinodal boundaries were determined in part from meteorite compositional data.

In Fe meteorites that have been studied, the local composition does not reach above ~ 50 wt pct Ni at the temperatures where the γ_2 forms. Therefore, no composition data were obtained by Reuter *et al.*^[5] with regard to the tricritical point, γ_2 eutectoid temperature, or $\gamma'' + \gamma'$ phase boundaries. These phase fields, above ~ 50 wt pct Ni, were calculated by Chuang *et al.*^[6] and used in the phase diagram (Figure 2), although the Fe-Ni phase diagram above ~ 50 wt pct Ni is not relevant to our investigation of Fe-Ni martensite decomposition. For a detailed discussion of this phase diagram, the reader is referred to Reuter *et al.*^[5]

According to this phase diagram, the equilibrium high

J. ZHANG, formerly Research Assistant, Department of Materials Science and Engineering, Lehigh University, is Staff Scientist, 3M Company, St. Paul, MN 55144. D.B. WILLIAMS, Professor, is with the Department of Materials Science and Engineering, Lehigh University, Bethlehem, PA, 18015-3195. J.I. GOLDSTEIN, Professor, is with the Department of Mechanical Engineering, University of Massachusetts, Amherst, MA 01003.

Manuscript submitted October 23, 1992.

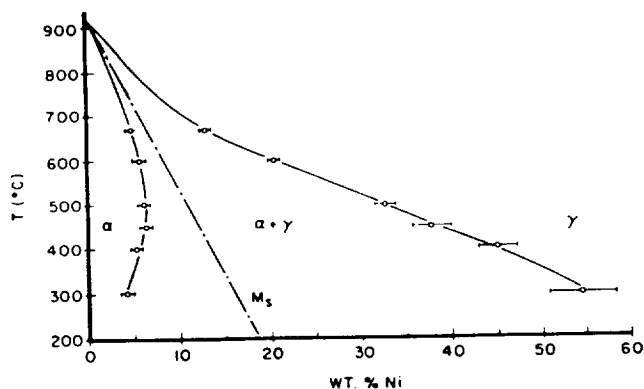


Fig. 1—Fe-rich portion of the low-temperature Fe-Ni phase diagram.^[12] The martensite start temperature, M_s , was measured by Kaufman and Cohen.^[11]

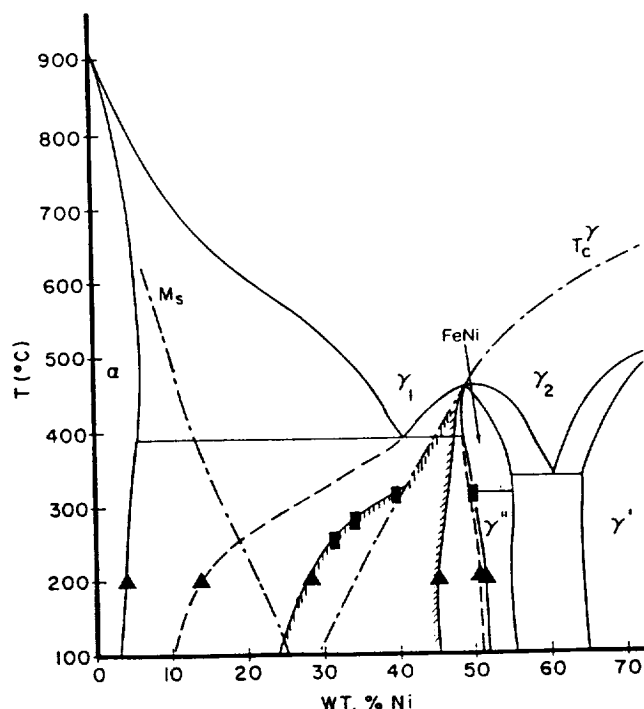


Fig. 2—Fe-Ni phase diagram proposed by Reuter *et al.*^[13] based on the investigation of iron meteorite structures, electron irradiated alloys, and the calculated Fe-Ni phase diagram by Chuang *et al.*^[16] The dotted/dashed line labeled M_s indicates the temperature below which martensite (α_2) forms. The dashed lines are metastable phase boundaries below 400 °C, which emanate from the tri-critical point, and the hatched lines delineate the spinodal decomposition region within the metastable two-phase field. The dotted/dashed line labeled T_c indicates the Curie temperature. Experimental data are shown as filled triangles from X-ray microanalysis of iron meteorites and as filled rectangles from electron irradiated alloys.

Ni phase produced by martensite decomposition below 400 °C should be γ'' (FeNi) either ordered or disordered, if an alloy is aged isothermally in the two-phase $\alpha + \gamma''$ phase field. The low Ni α phase, depending upon the aging temperature and alloy composition, could either be the equilibrium α phase or a metastable phase having a Ni composition specified by the miscibility gap. The structure of the metastable low Ni phase could be either

fcc or bcc (martensite) if the miscibility gap composition is lower than the M_s composition at a given temperature. Although this phase diagram successfully explains many observed structures in iron meteorites,^[14] there is no experimental evidence using laboratory alloys to evaluate the proposed phase diagram below 500 °C.

The purpose of this study is to examine the low-temperature martensite decomposition process using laboratory Fe-Ni alloys and measuring the composition of the phases in decomposed martensite by AEM.^[12] The great improvement in the X-ray spatial resolution of the AEM over the past 10 years permits much more accurate and reliable compositional data to be obtained.^[18] In addition, the results of the experimental studies will be used to establish the low-temperature (<500 °C) metastable Fe-Ni phase diagram. Fe-Ni alloys saturated with P in solid solution were also studied, because the ternary system controls the phase equilibria in iron meteorites, whose phase boundary data form a major component of the most recent phase diagram.^[17]

II. EXPERIMENTAL

A. Alloy Preparation

Alloys used in this study were made from high-purity (>99.99 wt pct) Fe and Ni rods and P particles. The Fe-Ni alloys were melted using a vacuum induction furnace (LEPEL* 3 kW high-frequency generator). The

*LEPEL is a trademark of Lepel Corporation, Edgewood, NY.

vacuum before melting was 5×10^{-6} torr or better. The molten metal was held in the liquid state for at least 30 seconds and slowly cooled in a few minutes to room temperature. The Fe-Ni-P alloys were melted under atmospheric pressure in an Ar environment to prevent severe loss of P during melting.

All the Fe-Ni and Fe-Ni-P alloys were homogenized in the single γ phase field at 1200 °C for 7 days. To prevent oxidation, each alloy was sealed in a quartz tube that was evacuated and refilled with argon gas. A piece of tantalum foil was placed in the tube as an absorber. After homogenization, the alloys were quenched first in water and then in liquid nitrogen to induce the martensite transformation. Each homogenized alloy was mounted, polished, and etched with 1 pct nital for metallographic examination. The homogeneity of each alloy was analyzed at the micrometer spatial resolution level using a JEOL733 EPMA. At least 16 measurements were made on random positions for each alloy specimen. The homogeneity range and homogeneity level were calculated using appropriate statistical equations.^[19] An alloy was considered homogeneous and used in the heat treatments if the homogeneity level of Ni was less than 1 pct at a 99 pct confidence level. The composition, homogeneity level, and microstructure, as observed in the optical microscope and the scanning electron microscope (SEM), of each alloy are listed in Table I. Each alloy is labeled by the first letter of the chemical symbol of its constituents and a number which is the nominal Ni composition in weight percent.

Each homogenous alloy was cut into 3-mm-diameter

Table I. Composition, Homogeneity Level, and Microstructure of As-Quenched Martensitic Alloys

Alloy	Ni (Wt Pct)	P (Wt Pct)	Homogeneity Level at 99 Pct Confidence Level Pct Ni	Microstructure
FN15	14.8	—	0.9	lath martensite
FN25	25.0	—	0.3	lath martensite
FN30	29.6	—	0.5	plate martensite
FNP15	14.9	0.24	0.4	lath martensite
FNP25	25.0	0.28	0.3	lath martensite
FNP30	30.6	0.27	0.8	plate martensite

rods for AEM specimens using a Servomet spark machine (Metals Research Ltd.). These alloy specimens were sealed separately in quartz tubes using the same procedure as that for alloy homogenization. The isothermal heat treatments were conducted in horizontal furnaces (Applied Test System Inc.) with an LFE model 2000 microprocessor temperature controller. The heat treatment temperatures were monitored using a separate K-type thermocouple that was placed next to the quartz tubes. The error of the heat treatment temperatures, determined by the accuracy of the thermocouple and the controller, was within $\pm 4^\circ\text{C}$ over time periods of up to 1 year. The alloys were quenched in water after the heat treatment was finished. All alloy specimens and their heat treatment times and temperatures are listed in Table II. A three digit number, which indicates the heat treatment temperature in degrees Celsius, is placed in front of the alloy label.

B. Structural and Compositional Analysis

Two SEMs, an ETEC AutoScan and a JEOL 840F, were used to observe the morphology of the decomposed martensite structure of each alloy. The specimens for SEM observation were polished and etched with 1 pct nital. The low Ni phase was preferentially etched.

Three AEMs were used to analyze the structure and the composition of the decomposed martensitic alloys. The AEMs included a PHILIPS* EM400T AEM equipped with an EDAX Si(Li) energy dispersive

spectrometer (EDS) detector and a Gatan 606 serial electron energy loss spectrometer (SEELS) controlled by a TRACOR NORTHERN** TN2000 EDS computer sys-

*PHILIPS is a trademark of Philips Electronic Instruments Corp., Mahwah, NJ.

**TRACOR NORTHERN is a trademark of Noran Instruments, Inc., Middleton, WI.

tem; a PHILIPS EM430T AEM equipped with a Link intrinsic Ge EDS detector and a Gatan 666 parallel electron energy loss spectrometer (PEELS) controlled by a Link AN10000 computer system; and a Vacuum Generators HB501 AEM equipped with a Link Si(Li) EDS detector and a Vacuum Generators SEELS controlled by a Link AN10000 computer system. The electron source was an LaB₆ filament for the PHILIPS AEMs and a cold field emission gun (FEG) for the HB 501. The accelerating voltage used was 120 kV for the EM400T, 300 kV for the EM430T, and 100 kV for the HB501. The electron probes formed by these AEMs have been systematically characterized in order to determine the spatial resolution of the X-ray analysis.^[10,11] The electron optical conditions used for the X-ray analysis were as follows: a 70- μm C2 aperture and an 8.5-nm-diameter full-width half-maximum (FWHM) probe for the EM400T; a 50- μm C2 aperture and a 7-nm-diameter (FWHM) probe for the EM430T; and a 50- μm virtual objective aperture and a 1-nm-diameter (FWHM) probe for the HB501. These were the optimum conditions under which the electron probe, formed at focus on the specimen, had a near-Gaussian intensity distribution. The electron probe resolutions approached the theoretically calculated values that consider the initial Gaussian diameter and the diameter of the disks of minimum confusion due to spherical aberration and diffraction from the probe-forming aperture.^[10]

The specimen thickness was measured using the X-ray standards technique.^[12] A calibration curve of X-ray counts/pA/min in a 0 to 10 keV range vs specimen thickness was made for each microscope using an Fe-25 wt pct Ni specimen.^[13] To obtain the calibration curves, the specimen thickness was measured using the EELS log-ratio method incorporating a parameterized equation for the total mean free path of inelastically scattered electrons.^[14] The typical thickness of the specimen regions, in which the EDS analysis was performed, was 40 to 100 nm for the PHILIPS AEMs and 10 to 30 nm for the VG AEM. Specimen drift was corrected manually for the EM400T AEM and was more accurately corrected for the HB501 AEM and the EM430T AEM by using a combination of digital image-storage and image-matching programs.

Table II. Heat Treatment Time and Temperature of Each Alloy

Martensite, Binary			Martensite, Ternary		
Alloy	T (°C)	t (Days)	Alloy	T (°C)	t (Days)
450FN15	450	60	450FNP15	450	60
450FN25	450	60	450FNP25	450	60
400FN15	400	362	400FNP15	400	362
400FN25	400	362	400FNP25	400	362
400FN30	400	362	400FNP30	400	362
370FN15	370	275	370FNP15	370	275
370FN25	370	275	370FNP25	370	275
370FN30	370	275	370FNP30	370	275
350FN15	350	400	350FNP15	350	208
350FN25	350	400	350FNP25	350	208
350FN30	350	400	350FNP30	350	208
300FN15	300	370	300FNP15	300	370
300FN25	300	370	300FNP25	300	370
300FN30	300	370	300FNP30	300	370

The Cliff–Lorimer ratio method,^[15] as given by,

$$C_A/C_B = k_{AB}(I_A/I_B) \quad [1]$$

was used to calculate the compositions, C_A and C_B , of the specimen-containing elements A and B from the measured X-ray intensities, I_A , I_B . For the analysis of Ni and Fe, the k_{NiFe} factors were measured for each instrument using a homogeneous Fe–Ni alloy of known composition. The absorption effect in the Fe–Ni system was negligible for the instrumental and specimen conditions used in this study. The spatial resolution of the X-ray analysis was calculated for the effect of electron probe size and beam broadening in the specimen.^[16,17] The X-ray spatial resolution, full-width tenth maximum (FWTM),^[18] obtained in this study was ~ 30 to 50 nm for the EM400T, ~ 10 nm for the EM430T, and ~ 2 nm for the HB501.

III. RESULTS

A. Structure of Decomposed Martensite

Figure 3 shows SEM secondary electron (SE) images that illustrate the morphologies of the decomposed martensite structure of various alloys. In the 15 and 25 wt

pct Ni alloys, the precipitates are formed in the martensite lath boundaries (Figures 3(a) and 3(b)) and are referred to as intergranular precipitates. This observation is confirmed by use of a transmission electron microscope (TEM) (Figure 4). Electron diffraction patterns show that the precipitate phase at the martensite lath boundaries is fcc, γ . Many more precipitates are formed in the 25 wt pct Ni alloys than in the 15 wt pct Ni alloys. The precipitates are smaller for the alloys heat-treated at lower temperatures, and no precipitates were observed in the 15 wt pct Ni alloy heat-treated at 300°C (300FN15).

Plate martensite was formed in the 30 wt pct Ni alloys, and upon aging precipitates were observed within the martensite plates and were referred to as intragranular precipitates. Figure 3(c) shows that the precipitates formed in an original martensite plate with a midrib in a 30 wt pct Ni alloy heat-treated at 400°C (400FN30). Typical widths of the precipitates are ~ 50 nm for the 30 wt pct alloy aged at 400°C and ~ 10 nm for the 30 wt pct alloy aged at 300°C (300FN30). The intragranular precipitates are also γ fcc phase and formed along several orientations (Figures 3(c) and (d)) in the parent martensite. Electron

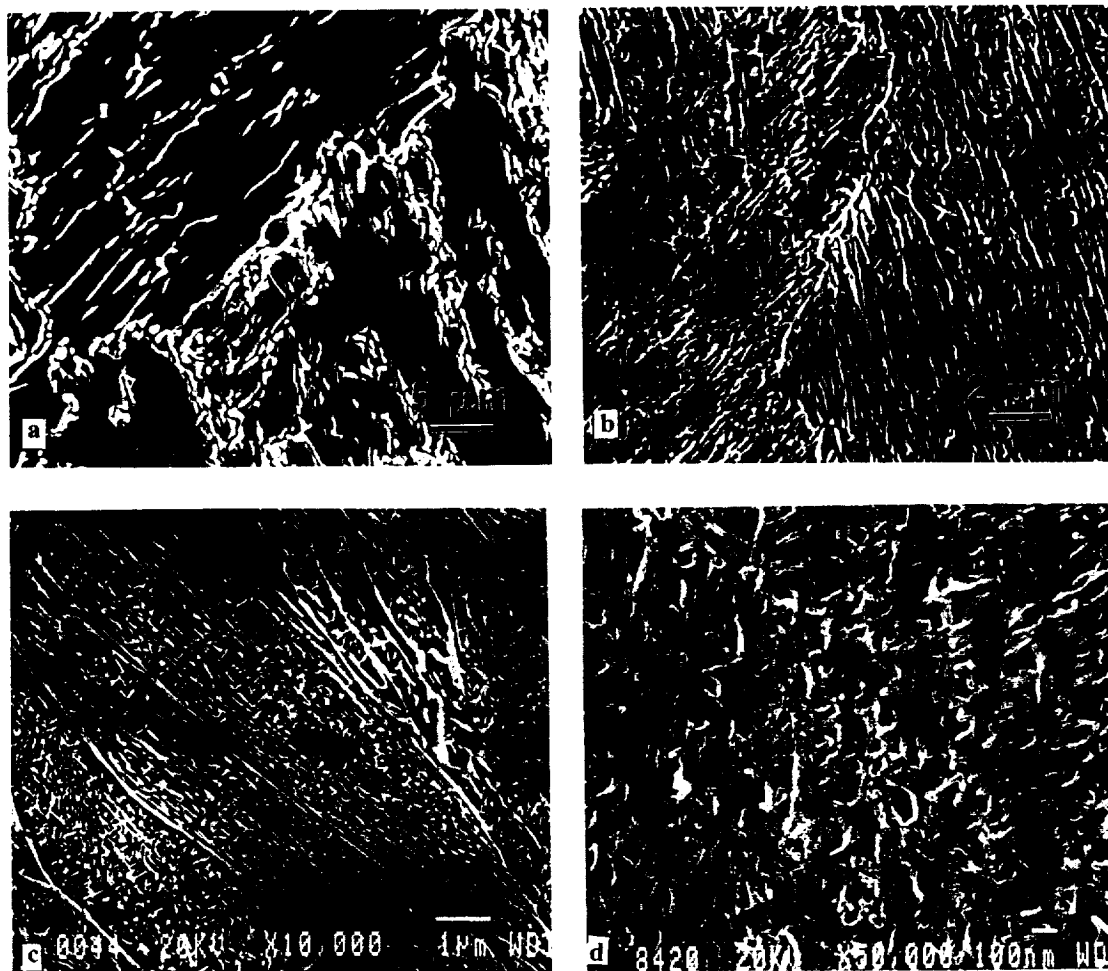


Fig. 3 — SEM secondary electron image of decomposed martensite in the following. (a) 15 wt pct Ni alloy aged at 450°C (450FN15). The arrow points out the precipitate phase. (b) 25 wt pct Ni alloy aged at 400°C (400FN25). The precipitate phase is unetched. (c) 30 wt pct Ni alloy aged at 400°C (400FN30). The precipitate phase is unetched. (d) 30 wt pct Ni alloy aged at 300°C (300FN30). The precipitate phase is unetched.

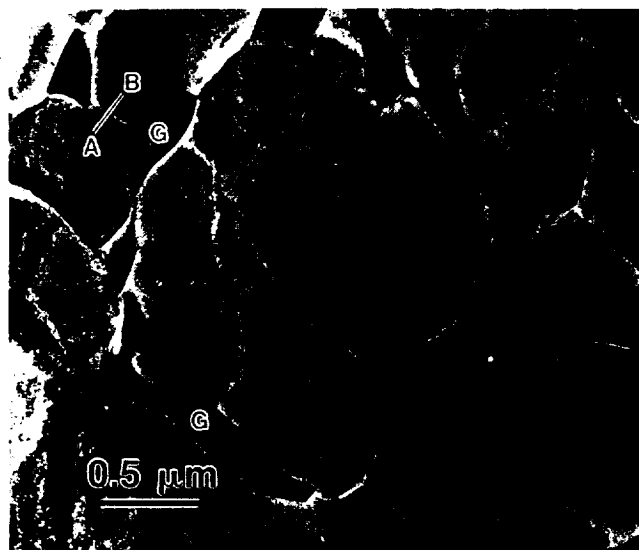


Fig. 4—TEM bright-field image of a 15 wt pct Ni alloy aged at 400 °C (450FN15) showing intergranular precipitates. *G* indicates the γ precipitates.

diffraction patterns show that these orientations are crystallographically equivalent orientations of the bcc structure of the matrix martensite, $\langle 110 \rangle_{\text{bcc}}$. The habit plane of the precipitates is $\{111\}_{\text{fcc}}$, and the habit plane is parallel to one of the $\{110\}_{\text{bcc}}$ planes. The orientation relationship of the γ precipitates in the martensite, $\{111\}_{\text{fcc}}/\{110\}_{\text{bcc}}$, is best described by a relaxed Nishiyama–Wasserman or Kurdjumov–Sachs orientation relationship; that is, the $\langle 110 \rangle_{\text{fcc}}$ is oriented between $\langle 100 \rangle_{\text{bcc}}$ and $\langle 111 \rangle_{\text{bcc}}$.

B. Compositional Data for Decomposed Martensite

Figure 4 is a TEM image of a 15 wt pct Ni alloy heat-treated at 450 °C (450FN15) showing intergranular precipitates. Nickel composition profiles across a γ precipitate and a martensite/martensite grain boundary along the path labeled A–B in Figure 4 are shown in Figures 5(a) and (b), respectively. The composition of the α matrix has not reached the equilibrium value of ~5 wt pct Ni. The Ni composition of the matrix area away from the precipitate is still at the bulk alloy composition (15 wt pct), and a composition gradient is present in the martensite matrix extending toward a precipitate/matrix interface and/or a grain boundary. The lowest matrix Ni composition is 7.6 ± 0.9 wt pct measured at a martensite grain boundary.

Figure 6 is a TEM image of a 30 wt pct Ni alloy heat-treated at 400 °C (400FN30) showing intragranular precipitates. A Ni composition profile across two precipitates in this alloy is shown in Figure 7. The measured composition profile is relatively flat and the matrix composition is above 10 wt pct Ni. The composition of the α matrix has not reached the equilibrium value of ~5 wt pct Ni. The extrapolated matrix composition at the precipitate/matrix interface is about 9.3 ± 0.5 wt pct Ni. No apparent Ni depletion zone is observed near the interface on a 10-nm scale, the spatial resolution of the X-ray analysis for this composition profile.

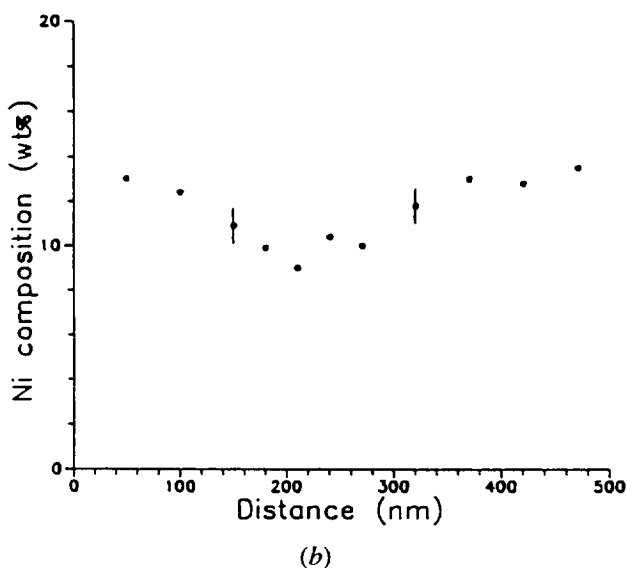
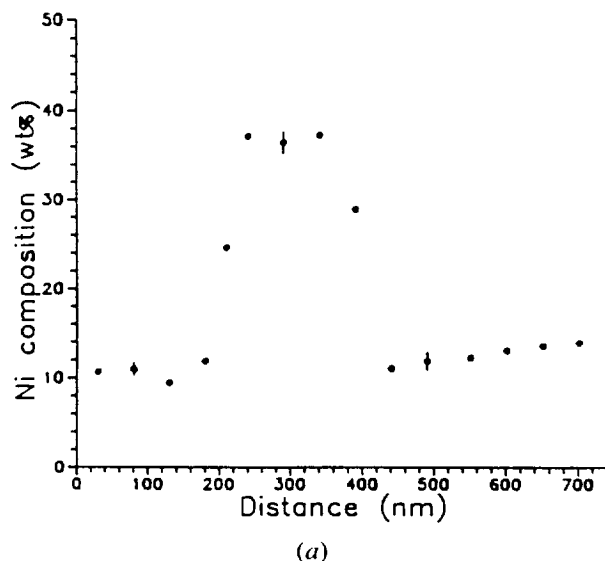


Fig. 5—EDS Ni composition profiles taken with the EM400T from alloy 450FN15 (Fig. 4). (a) Profile taken across an intergranular precipitate. (b) Profile taken across a grain boundary (line A–B in Figure 4).

C. Effects of Temperature, Structure, and Composition

Figure 8 shows TEM bright- and dark-field images ($g = \langle 111 \rangle_{\text{fcc}}$) of a γ precipitate in a 15 wt pct Ni alloy heat-treated at 370 °C (370FN15). The contamination spots formed during the X-ray analysis across the precipitate (up to 3 minutes counting time) can be seen on the bright-field image. The regularly spaced small bright dots barely seen in the precipitate/matrix interface in the dark-field image, as shown by the arrow in Figure 8(b), can be interpreted as the interfacial dislocations characteristic of a semicoherent interface. The Ni composition profile across this precipitate is shown in Figure 9. Most areas of the matrix still remain at the original Ni content of 15 wt pct. The composition gradient toward the precipitate/matrix interface is very small.

Figure 10 is a Ni composition profile across several



Fig. 6—TEM bright-field image of a 30 wt pct Ni alloy aged at 400 °C (400FN30) showing intragranular precipitates. *G* indicates the γ precipitates.

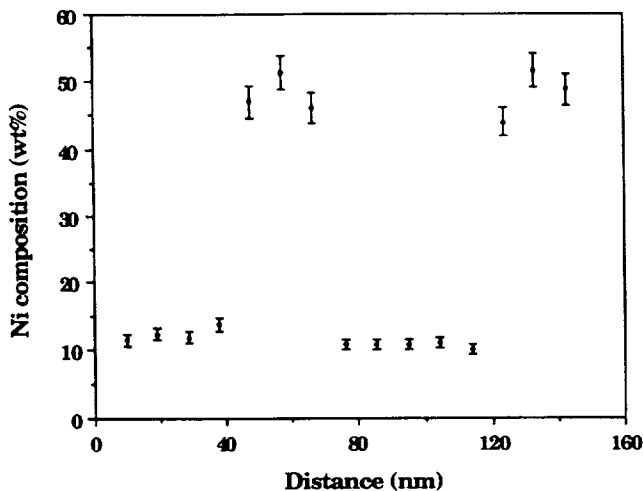


Fig. 7—EDS Ni composition profile taken across two γ precipitates with the EM400T from alloy 400FN30 (Fig. 6).

precipitates measured in the 30 wt pct Ni alloy heat-treated at 350 °C (350FN30). Significant variation in the matrix composition was observed in this composition profile and in composition profiles from other alloys. Measurements using well-characterized electron optical and specimen conditions from several locations of varying thickness in the same alloy show that the variation in the matrix Ni composition was not due to analytical error or to varying specimen thickness. Figure 11 shows a TEM bright-field and a dark-field image ($g = \langle 111 \rangle_{fcc}$) of the 30 wt pct Ni alloy heat-treated at 300 °C (300FN30). The precipitate structure is the same as that shown in Figure 6. However, the precipitates in this alloy are only ~10-nm wide, and it is more difficult to separate the fcc reflections of the precipitates from the bcc reflections of the matrix in the electron diffraction pattern, indicating a higher degree of coherence of the microstructure. A Ni composition profile across a precipitate in this alloy (300FN30) is shown in Figure 12.



Fig. 8—(a) TEM bright-field image of a 15 wt pct Ni alloy aged at 370 °C (370FN15). (b) Centered dark-field images of a $(111)_{fcc}$ diffraction spot and a $(110)_{bcc}$ diffraction spot that are too close to each other to be separated by the aperture. Interfacial dislocations observed are indicated by the arrow.

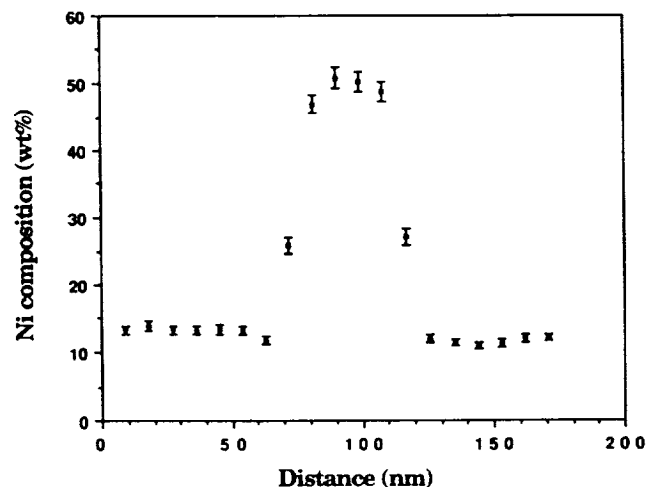


Fig. 9—EDS Ni composition profile taken with the EM 430T across an intergranular precipitate in a 15 wt pct Ni alloy aged at 370 °C (370FN15) (Fig. 8).

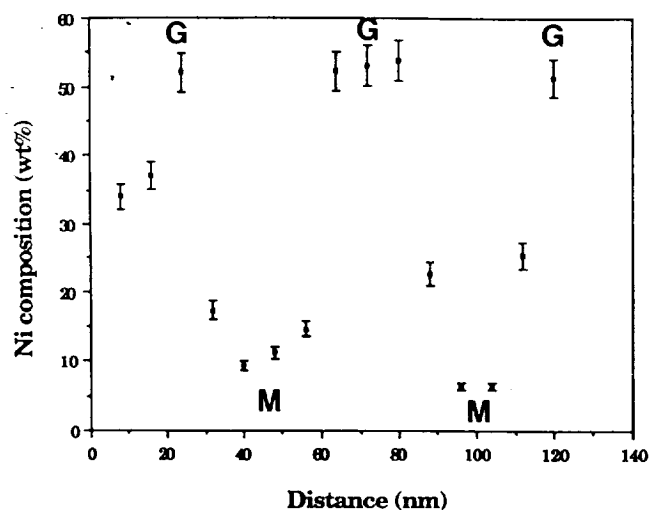


Fig. 10 — EDS Ni composition profile taken with the EM 430T across several intragranular precipitates in a 30 wt pct Ni alloy aged at 350 °C (350FN30). *G* indicates the γ precipitates. *M* indicates the matrix.

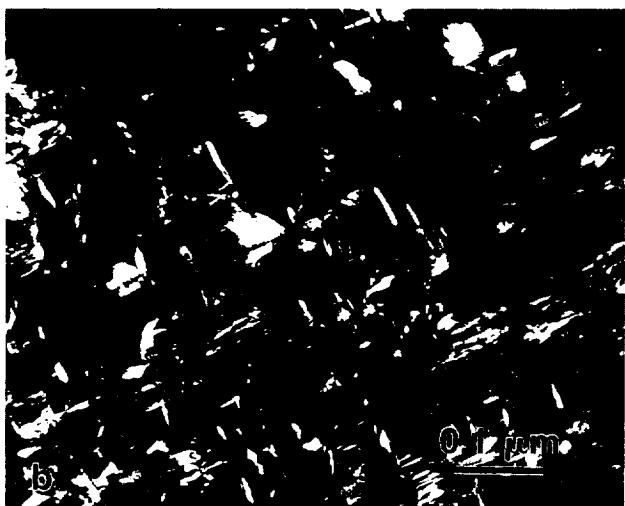
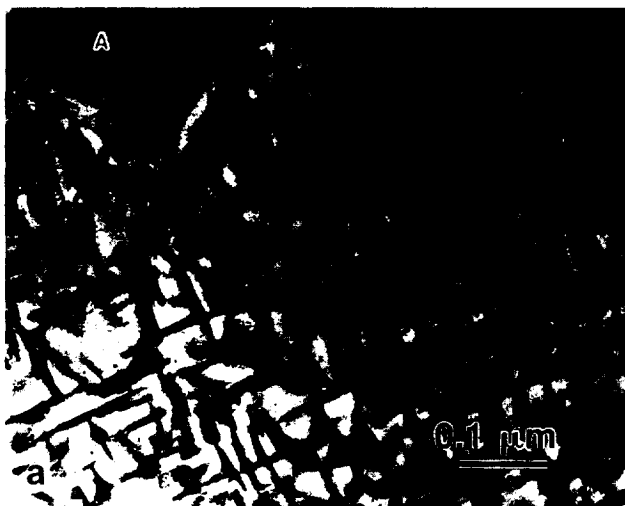


Fig. 11 — (a) TEM bright-field image of a 30 wt pct Ni alloy aged at 300 °C (300FN30). (b) Centered dark-field image of a weak fcc diffraction spot. Moiré fringes are observed.

The composition variation in the α phase is small, and the interface composition measured in the matrix is much higher than the equilibrium Ni content in the α phase of ~ 4 wt pct. The interface between precipitate and matrix is at a distance of 12.5 nm (Figure 12) assuming an X-ray spatial resolution of ~ 2.5 nm.

The precipitate composition and the lowest matrix Ni composition measured near the matrix/precipitate interface or the grain boundary in each binary alloy are listed in Table III. In addition, phase composition data obtained using the atom probe field ion microscope for alloy 300FN25⁽¹⁸⁾ are also listed in Table III. The error associated with each composition in Table III is the statistical error in the X-ray counts. Several of the analyses as noted in Table III, however, have large errors because the precipitate size is at or below the X-ray spatial resolution of the AEM employed for the analysis. The γ precipitate compositions measured in alloys of different composition, but aged at the same temperature, show

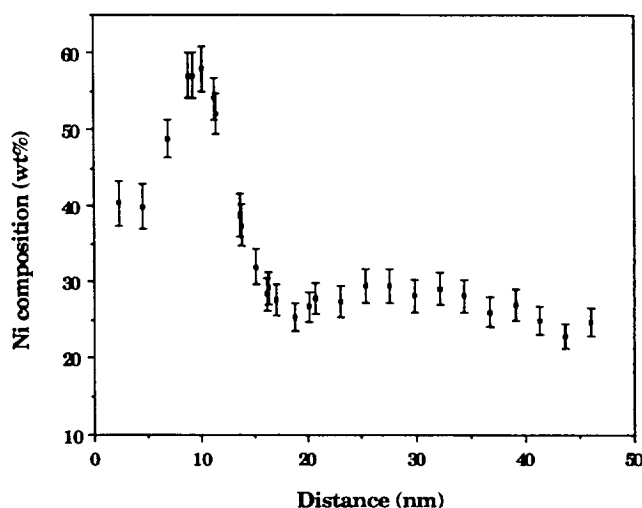


Fig. 12 — EDS Ni composition profile taken with the HB501 across an intragranular precipitate in a 30 wt pct Ni alloy aged at 300 °C (300FN30) (Fig. 11).

Table III. Ni Compositions of Precipitate and Matrix Phases in Binary Alloys (Wt Pct)

Alloy	Precipitate (γ)	Matrix (α)	Instrument
450FN15	39.7 ± 0.8	7.6 ± 0.9	EM400T
450FN25	39.6 ± 1.3	9.4 ± 0.5	EM430T
400FN15	48.2 ± 1.3	8.5 ± 0.8	EM400T
400FN25	49.8 ± 1.7	13.2 ± 1.8	EM400T
	50.6 ± 1.5	9.1 ± 0.5	HB501
400FN30	50.9 ± 2.1	9.3 ± 0.5	EM430T
370FN15	50.9 ± 1.7	9.1 ± 0.5	EM430T
370FN25	49.8 ± 3.9	15.0 ± 2.0	EM430T
370FN30	52.7 ± 2.2	12.4 ± 0.7	EM430T
350FN15	52.0 ± 1.7	10.0 ± 0.7	EM430T
350FN25	~ 42	~ 18	EM430T*
350FN30	52.0 ± 2.8	5.6 ± 0.7	EM430T
300FN25	50.8 ± 2.3	20.5 ± 1.0	HB501
	58 ± 11	20 ± 1.9	atom probe
300FN30	57.4 ± 3.0	21.0 ± 1.6	HB501

*Not accurate; precipitates are too small for EM430T.

good consistency. However, the matrix (α) compositions and the precipitate/matrix interface compositions show significant variation among alloys aged at the same temperature and at different locations in the same alloy. The composition profiles measured in the matrix are relatively flat and have precipitate/matrix interface Ni compositions higher than those predicted in the phase diagram. The measured precipitate and matrix compositions listed in Table III, except those compositions where the X-ray spatial resolution was inadequate, are plotted on the Reuter *et al.* Fe-Ni phase diagram (Figure 13). The error bar for each point in this diagram is the range of variation for the measurements made at different locations in the same alloy and alloys of different Ni composition aged at the same temperature.

The measured Ni composition of the γ precipitates and martensite matrix of the ternary (Fe-Ni-P) alloys are listed in Table IV. The microstructures of the ternary alloys are very similar to their binary counterparts except for the presence of the $(\text{Fe-Ni})_3\text{P}$ precipitates. The solubility of P in both α and γ Fe-Ni phases is very low (<0.2 wt pct) and could not be measured by the EDS

detector. The measured Ni composition profiles in the ternary alloys show the same characteristics as those of their binary counterparts. The Ni compositions of the γ precipitates in the ternary alloys are slightly lower than those in the binary alloys. The difference in matrix composition between the ternary and the binary alloys is smaller than the composition variation in the matrix itself. The errors in Table IV are the statistical errors calculated from the X-ray counts of one measurement.

IV. DISCUSSION

A. Structure and Composition of Decomposed Martensite

For alloys with 15 and 25 wt pct Ni aged between 300 °C and 450 °C, lath martensite decomposed with γ (fcc) precipitates forming intergranularly at the lath boundaries. For alloys with 30 wt pct Ni aged between 300 °C and 450 °C, plate martensite decomposed with γ (fcc) precipitates forming intragranularly within the martensite plates. The habit plane for the precipitates is $\{111\}_{\text{fcc}}$ parallel to one of the $\{110\}_{\text{bcc}}$ planes in the martensite.

The composition of the γ intergranular and intragranular precipitates formed between 300 °C and 400 °C is quite similar. The Ni contents all lie between 48 and 58 wt pct and generally increase in Ni content with decreasing temperature (Table III). The Ni contents of γ phase all lie at somewhat higher Ni contents than those given by the current Fe-Ni phase diagram^[7] (Figures 2 and 13). The Ni composition of the martensite, bcc, matrix is well above the equilibrium value of 4 to 5 wt pct. Diffusion gradients are observed in the matrix with decreasing Ni contents close to the martensite grain boundaries and matrix/precipitate boundaries. The minimum Ni content of the matrix was measured as close to the matrix/ γ interface as allowed by the X-ray spatial resolution of the AEM (Table III). Almost all the matrix minimum Ni contents measured are well above the equilibrium α (bcc) phase composition. All the compositional data therefore point to the development of nonequilibrium interface compositions during the decomposition of martensite (300 °C to 400 °C).

B. The Growth Process for Decomposed Martensite

The most common growth mechanism for precipitation is diffusion-controlled growth in which the rate-limiting step is volume diffusion of the solute atoms to the precipitate/matrix interface.^[19] Figure 14 shows typical composition profiles of composition X_B vs distance for the growth of a precipitate β in a matrix of α phase at various stages of growth (t_1 , t_2 , final state). For diffusion control (Figure 14), the compositions of the precipitate, β , and the matrix, α , at the β/α interface in an alloy of composition, X_0 , are the equilibrium values, X_β and X_α , during the growth process. There is, however, a composition gradient in the matrix α toward the interface. After growth is completed (final state), the compositions of the precipitate, β , and the matrix, α , are X_β and X_α and there are no diffusion gradients in the matrix phase. The Ni composition of the γ'' and α phases in

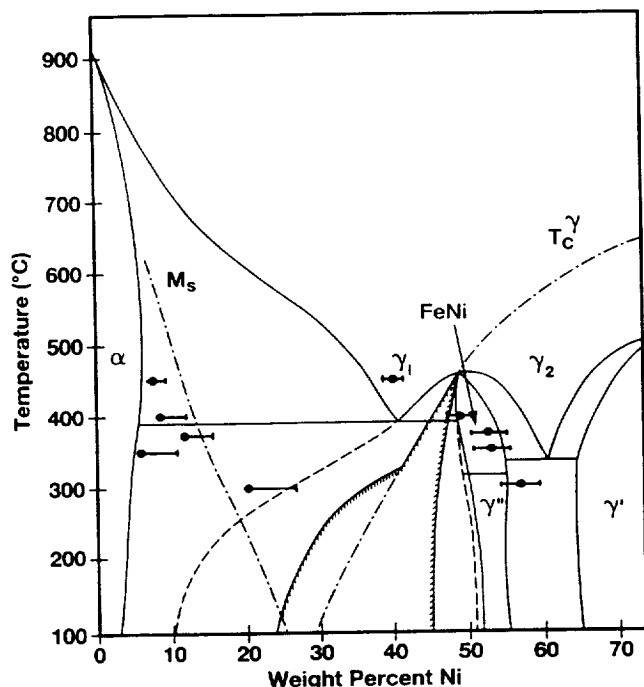


Fig. 13—Measured composition data for the γ precipitates and matrix α from aged martensite alloys (Table III) plotted on the Fe-Ni phase diagram of Reuter *et al.*^[5] (Fig. 2).

Table IV. Ni Compositions of Precipitate and Matrix of the Fe-Ni Phases in the Ternary Alloys (Weight Percent)

Alloy	Precipitate (γ)	Matrix (α)	Instrument
450FNP15	39.2 \pm 0.5	12.2 \pm 0.7	EM400T
400FNP15	48.7 \pm 2.7	12.7 \pm 0.6	EM400T
400FNP25	46.9 \pm 1.1	13.9 \pm 0.7	EM400T
370FNP25	49.1 \pm 1.5	12.2 \pm 0.6	EM430T
350FNP30	50.2 \pm 2.6	17.1 \pm 1.2	EM400T
300FNP30	54.1 \pm 1.0	23.0 \pm 0.8	HB501

decomposed martensite from the experimental alloys of this study is significantly higher than the equilibrium values. Therefore, precipitate growth in decomposed martensite (300 °C to 400 °C) is not diffusion-controlled (Figure 14) and an alternative mechanism is required to explain the observations.

Interface controlled growth is an alternative process, in which the rate-controlling mechanism is the movement of the interface between precipitate and matrix rather than volume diffusion of solute atoms through the matrix to the interface. Figure 14 illustrates the composition gradients developed when the growth rate is interface-controlled. The interface composition is higher than the equilibrium value during growth, and there is no composition gradient in the matrix. To a first approximation, the maximum velocity of the interface is determined by the difference in chemical potential across the interface. At equilibrium (final state), the velocity of the interface is zero. Typically, interface controlled growth occurs on the flat interfaces of plate-shaped precipitates that are semicoherent. Under these circumstances, some form of ledge (dislocation) mechanism is usually postulated to account for the slow thickening of the precipitates.^[20,21] Since the Ni content for the matrix phase in decomposed martensite, at the precipitate/matrix interface from the experimental alloys of this study, is higher than the equilibrium value, interface control may be responsible for precipitate growth. However, since a diffusion gradient is still measured in the

matrix of some alloys (Figure 5), partial interface control, as shown in Figure 14, may control the growth process.

Before concluding that growth is interface-controlled, it is important to understand how lengthwise growth of the precipitate occurs and how the composition of the precipitate and matrix adjust to lengthwise growth. In lengthwise growth of precipitates, the interfaces at the ends of the precipitate are likely to be incoherent^[22] and have a high mobility. Lengthwise growth may often be diffusion-controlled.^[22] However, the composition of the matrix in equilibrium with the ends of the precipitate will be increased by the phenomenon of capillarity, which is also known as the Gibbs–Thompson effect. The basic equation that describes the increase of the matrix composition is

$$X_r = X_{00} \exp \{ (2\Gamma V_m / RT r) * (1 - X_{00}) / (X_p - X_{00}) \} \quad [2]$$

where X_r is the solute composition of the matrix phase at the tip of the precipitate of radius r , X_{00} is the solute composition of the matrix phase at the tip of the precipitate of radius infinity (plate-shaped precipitate), Γ is the interfacial energy, V_m is the molar volume, R is the gas constant, T is the absolute temperature, and X_p is the solute composition of the precipitate phase.^[23] The net effect of capillarity is that the smaller the radius of curvature of the precipitate, the higher the composition of the surrounding matrix.

One possible scenario for the growth of the γ precipitate is that the precipitate growth is entirely due to lengthwise growth and that the interface growth rate of the flat interface is essentially zero because of the slow ledge growth mechanism. In this scenario, the matrix composition at the flat interface will be inherited from the matrix composition determined by the capillarity effect at the growing tip of the precipitate. A model of this type of growth is shown schematically in Figure 15(a). The tip radius is assumed to remain constant as the edge-wise growth occurs and the flat interface remains at the same position during growth. Using measured values of X_p , X_r , and X_{00} of 0.57, 0.21, and 0.05, a growth temperature T of 573 K for alloy 300FN30, a typical value for Γ for an incoherent interface of 0.3 J/m², and a molar volume V_m of 7×10^{-6} m³, the calculated radius, r , of the precipitate tip from Eq. [2] is ~ 1 nm. The measured width of such a γ precipitate is approximately 10 nm, which is much larger than the calculated width considering capillarity. Such a simple growth model of edge-wise growth cannot explain the formation of the

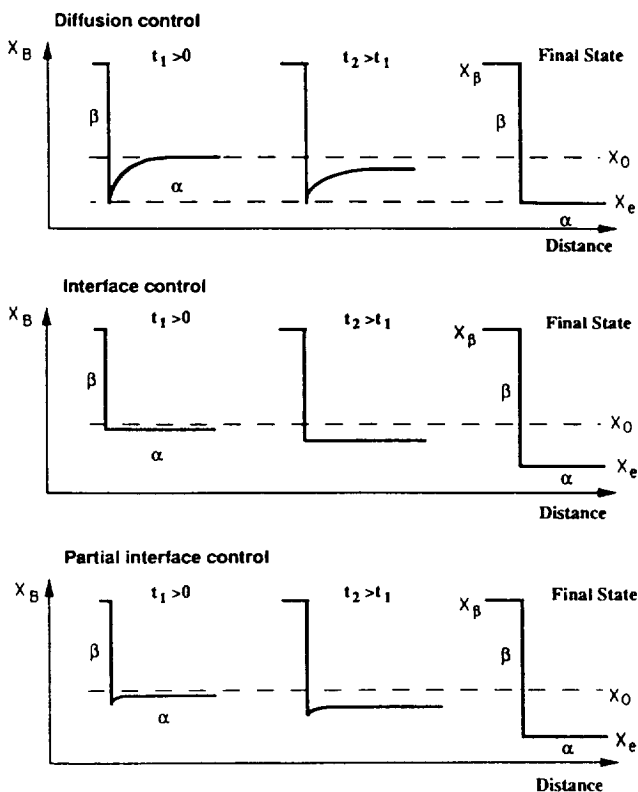


Fig. 14—Schematic concentration gradients developed for β precipitate growth by α -diffusion-control, interface reaction-control, and partially interface reaction-control. X_0 is the bulk composition, and X_β and X_α are the equilibrium compositions of β and α , respectively.

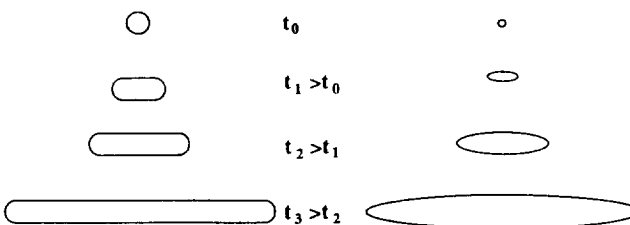


Fig. 15—Schematic drawing of (a) precipitate growth due entirely to lengthwise growth (interface growth rate of the flat interface is zero) and (b) precipitate growth due to a combination of lengthwise growth and thickening of the flat interface. Precipitate thickening is controlled by a combination of interface- and diffusion-controlled growth.

microstructure and the high Ni matrix composition of the γ precipitate. This model is probably also unrealistic because it requires a constant value of r , which is quite large for the initial size of the nucleus of a precipitate.

Accordingly, we propose a model for precipitate growth which is shown schematically in Figure 15(b). In this model, the critical radius of the nucleus is smaller in the initial stages and therefore the Ni content in the matrix given by the capillarity effect is larger than the experimentally observed value. This higher Ni composition allows for thickening of the small nuclei. As growth proceeds, the precipitate not only lengthens rapidly but also thickens, to a much smaller extent, by some combination of interface and diffusion-controlled growth. As the radius of the precipitate tip increases, the Ni concentration in the matrix surrounding the lengthening precipitate decreases toward the observed value, e.g., ~21 wt pct for experimental alloy 300FN30. The matrix composition between the growing precipitates will also decrease toward the observed Ni content. This growth process is illustrated in Figure 14 for partial interface control. As the matrix composition decreases toward the observed Ni level, the interface motion of the flat interface slows considerably. A result of this process is that the matrix will not reach the equilibrium composition (final state) within the time available. This growth process results in the matrix Ni content being fixed at the observed Ni content which is between that of the initial stage, t_1 , and that expected for the final stage, as shown in Figure 14.

The Ni composition of the fine intragranular precipitates is ~5 wt pct Ni higher than the equilibrium Ni content of FeNi, γ'' (Figures 2 and 13). One possible reason for the higher Ni content of the precipitates is that the capillarity effect may also increase the Ni content, not only of the matrix phase but also of the intragranular precipitates. Unfortunately, it is difficult to calculate the magnitude of the capillarity effect on the intragranular precipitates.

The experimental data suggest that the precipitate growth in Fe-Ni martensite decomposition at low temperatures (<500 °C) is partially interface reaction-controlled. To support this argument, a more quantitative approach is presented in a companion article in which the precipitate growth is numerically simulated by both diffusion-controlled and interface-controlled models.^[24] This study shows that a partial interface reaction-controlled model gives simulated Ni profiles that approximate the experimentally measured Ni profiles.^[11,24]

C. Metastable and Equilibrium Fe-Ni Phase Diagram at Low Temperatures (<500 °C)

As shown in Figure 13, the measured phase equilibria in the decomposed martensitic alloys are quite different from what is predicted in the current Fe-Ni phase diagram.^[7] The current Fe-Ni phase diagram contains not only equilibrium phase boundaries but also metastable boundaries, for example, miscibility gap and spinodal lines, as well as the martensite start line. In many cases, the products of metastable phase transformations are preserved and are observed in the laboratory and in meteorite specimens.

The measured matrix compositions, as discussed in detail previously, are intermediate states during the martensite decomposition. The precipitate/matrix composition before the alloy is fully equilibrated cannot be used to determine any phase boundary because of the interface reaction-controlled growth mechanism. The degree of the interface reaction control decreases as the temperature increases. At higher temperatures, the precipitate/matrix composition should be close to the equilibrium phase boundary value. Although the transition from mostly diffusion control at higher temperatures to mostly interface control at lower temperatures is gradual, the transition occurs between 450 °C and 400 °C for the Fe-Ni alloys. The interface composition measured in the 450 °C alloys is close to the values given in the phase diagram.

The composition of the precipitates formed at each temperature is consistent among alloys of different composition and does not show a large variation with the local microstructure. Therefore, the precipitate compositions measured are the stable states formed by martensite decomposition, although they may not be at the final equilibrium composition.

The equilibrium $\gamma/\alpha + \gamma$ phase boundary at 450 °C can be modified according to the measured precipitate composition in this study (~40 wt pct Ni). There is about a 10 wt pct difference in the precipitate Ni composition at 450 °C and 400 °C, whereas the difference between 400 °C and 350 °C is minimal (Figure 13). These differences indicate that the eutectoid temperature should be between 450 °C and 400 °C instead of the calculated value of 394 °C.^[6]

Below 320 °C, the phase diagram predicts an ordered phase, FeNi. Although the atomic electron scattering factors of Fe and Ni are nearly equal, superlattice reflections have been observed for the ordered $L1_0$ structure of the ordered phase FeNi, γ'' , in iron and stony iron meteorites.^[14,25] However, no ordering was observed in this study for the 300 °C alloys using electron diffraction techniques. The precipitate Ni composition measured in the 300 °C alloy is ~57 wt pct, significantly higher than the stoichiometric FeNi composition. The failure of the precipitate composition to follow the $\alpha + \gamma''/\gamma''$ phase boundary indicates the separation of the phase equilibria formed through different phase transformations. While the current Fe-Ni phase diagram is valid for the phase equilibrium formed by nucleation of α in a γ matrix, as in the iron meteorites, the phase equilibrium formed by martensite decomposition follows another phase boundary that appears to be an extension of the high-temperature $\gamma/\gamma + \alpha$ boundary. It is interesting to note that in iron meteorites, the ordering transformation occurs in the γ'' precipitates. The Ni composition of the precipitates is ~52 wt pct (FeNi) or >57 wt pct depending on whether the precipitates are formed at high or low temperature.^[25] Therefore, the phase transformation process in Fe-Ni alloys at low temperatures is a kinetically governed process, and the phase equilibria are strongly affected by the transformation sequence. The precipitate compositions measured in this study are determined by martensite decomposition. The final equilibrium state may be γ'' (FeNi) plus a low Ni α phase. However, the phase

boundary compositions may not be the same at low temperatures for the decomposition of martensitic alloys or the decomposition of austenitic alloys. It also appears that the ordering transformation (ordering temperature ~ 320 °C) to form γ'' (FeNi) is a much slower process compared with martensite decomposition.

V. SUMMARY

1. Phase structure and compositions, for Fe-Ni and Fe-Ni(P) alloys heat-treated from 450 °C to 300 °C and formed by isothermal martensite decomposition, are established. No significant difference is observed between the binary and the ternary alloys at these low temperatures.
2. The phase structures measured in this study belong to various metastable states at low temperatures. The ordered fcc phase, FeNi, is not observed in these alloys. The precipitate compositions at low temperatures are stable in terms of the martensite decomposition and metastable relative to the final equilibrium state (without FeNi ordering). Most matrix compositions are metastable even with regard to the martensite decomposition as a consequence of the interface-controlled precipitate growth in these alloys.
3. It is shown that the phase structure and compositions of the Fe-Ni alloys are different at low temperatures for different transformation paths due to the kinetics of the phase transformations. The current Fe-Ni phase diagram is in agreement with the decomposition of the austenite phase. According to the data of this study, the $\gamma/\alpha + \gamma$ phase boundary in the Romig phase diagram is revised and the eutectoid reaction^[6,7] occurs between 400 °C and 450 °C.

ACKNOWLEDGMENTS

This research was supported by NASA through Grant No. NAG 9-45. The authors would like to thank Dr. J.R. Michael of Homer Research Laboratory, Bethlehem Steel Corporation (now at Sandia National Laboratories), and Dr. C.E. Lyman of Lehigh University for the assistance with the VG STEM.

REFERENCES

1. L. Kaufman and M. Cohen: *Trans. AIME*, 1956, vol. 206, pp. 1339-401.
2. A.D. Romig, Jr. and J.I. Goldstein: *Metall. Trans. A*, 1980, vol. 11, pp. 1151-59.
3. J.I. Goldstein and R.E. Ogilvie: *Trans. AIME*, 1965, vol. 233, pp. 2083-87.
4. K.B. Reuter, D.B. Williams, and J.I. Goldstein: *Geochim. Cosmochim. Acta*, 1988, vol. 52, pp. 617-26.
5. K.B. Reuter, D.B. Williams, and J.I. Goldstein: *Metall. Trans. A*, 1989, vol. 20, pp. 711-18.
6. Y.Y. Chuang, Y.Y. Chang, R. Schmid, and J.C. Lin: *Metall. Trans. A*, 1986, vol. 17, pp. 1361-72.
7. K.B. Reuter, D.B. Williams, and J.I. Goldstein: *Metall. Trans. A*, 1989, vol. 20, pp. 719-25.
8. D.B. Williams, J.R. Michael, J.I. Goldstein, and A.D. Romig: *Ultramicroscopy*, 1992, vol. 47, pp. 121-32.
9. J.I. Goldstein, D.E. Newbury, P. Echlin, D.C. Joy, A.D. Romig, C.E. Lyman, C. Fiori, and E. Lifshin: *Scanning Electron Microscopy and X-Ray Microanalysis*, 2nd ed., Plenum Press, New York, NY, 1992, pp. 493-97.
10. J.R. Michael: *Microbeam Analysis—1988*, San Francisco Press Inc., San Francisco, CA, 1988, pp. 60-64.
11. J. Zhang: Ph.D. Dissertation, Lehigh University, Bethlehem, PA, 1991.
12. D.A. Porter and H. Westengen: *Quantitative Microanalysis with High Spatial Resolution*, G.W. Lorimer, M.H. Jacobs, and P. Doig, eds., The Metals Society, London, 1981, pp. 94-100.
13. J.I. Goldstein, C.E. Lyman, and J. Zhang: *Microbeam Analysis—1990*, San Francisco Press Inc., San Francisco, CA, 1990, pp. 265-73.
14. T. Malis, S.C. Cheng, and R.F. Egerton: *J. Electron Micro. Technol.*, 1988, vol. 8, pp. 193-200.
15. G. Cliff and G.W. Lorimer: *J. Microsc.*, 1975, vol. 103, pp. 203-07.
16. S.J.B. Reed: *Ultramicroscopy*, 1982, vol. 7, pp. 405-09.
17. J.R. Michael, D.B. Williams, C.F. Klein, and R. Ayer: *J. Microsc.*, 1990, vol. 160, pp. 41-53.
18. J. Zhang, M.K. Miller, D.B. Williams, and J.I. Goldstein: *Surf. Sci.*, 1992, vol. 266, pp. 433-40.
19. P. Haasen: *Physical Metallurgy*, 2nd ed., Cambridge University Press, Cambridge, United Kingdom, 1986, pp. 211-15.
20. H.I. Aaronson: *Decomposition of Austenite by Diffusional Process*, 1962, Interscience, New York, NY, pp. 387-548.
21. R.D. Doherty: *Physical Metallurgy*, R.W. Cahn and P. Haasen, eds., North-Holland Publishing, Amsterdam, 1983, pp. 966-75.
22. D.A. Porter and K.E. Easterling: *Phase Transformations in Metals and Alloys*, Van Nostrand Reinhold, Wokingham, Berkshire, United Kingdom, 1981, pp. 279-87.
23. J.W. Martin and R.D. Doherty: *Stability of Microstructure in Metallic Systems*, Cambridge University Press, Cambridge, United Kingdom, 1976, pp. 36-50.
24. J. Zhang, D.B. Williams, and J.I. Goldstein: *Metall. Mater. Trans. A*, 1994, vol. 25A, pp. 1639-48.
25. J. Zhang, D.B. Williams, and J.I. Goldstein: *Geochimica et Cosmochimica*, 1993, vol. 57, pp. 3725-35.

